Journal of Physics: Materials

CrossMark

Seeking borophene on Ni₃Al(111): an experimental characterization of boron segregation and oxidation

Y Y Grisan Qiu[1], P Biasin[1], P Mantegazza[1], S Baronio[1], M Heinrich[2,3], M K Muntwiler[2] and E Vesselli[1,4,5,*]

1 Department of Physics, University of Trieste, 34127 Trieste, Italy
2 Paul Scherrer Institut, Villigen 5232, Switzerland
3 Swiss Nanoscience Institute, University of Basel, 4056 Basel, Switzerland
4 CNR-IOM, Istituto Officina dei Materiali, 34149 Trieste, Italy
5 Center for Energy, Environment and Transport Giacomo Ciamician, University of Trieste, 34127 Trieste, Italy
* Author to whom any correspondence should be addressed.

E-mail: vesselli@iom.cnr.it and evesselli@units.it

Abstract

Synthesis of a stable, well ordered honeycomb borophene (hB) phase has been achieved to date by exploiting Al(111) as a growth substrate, which provides the necessary charge doping to compensate the high hexagonal-holes density. However, B/Al(111) is governed by a strong B–Al interaction so to yield the actual formation of an AlB₂ hB phase. Dilution of aluminum by alloying could then in principle weaken the boron-support bonding. By means of a combined spectroscopy and microscopy experimental approach, we find instead that the growth of boron layers on the Ni₃Al(111) alloy termination is driven by B dissolution into the bulk and surface segregation mechanisms. While no long-range ordered boron-induced phase is observed, locally ordered superstructural units with triangular appearance are stabilized by substrate pinning, following the chemical $p(2 \times 2)$ surface order. Oxidation involves both boron and aluminum, inducing surface segregation of B, while nickel remains in its metallic form.

1. Introduction

The boron atom displays three valence electrons with a short $2p$ radius, close to that of the $2s$ level and, thus, yielding localized states. This translates in the multicentric bonding character of boron, at the origin of a variety of stable bonding geometries involving covalent two-centers bonds and multi-centric coordination with metallic flavor. Since the trivalent outer shell of boron cannot support closed shell structures, energy is minimized by highly delocalized bonding through shared electron pairs. Consequently, elemental boron forms several bulk polymorphic allotropes based on interconnected B₁₂ icosahedral units as building blocks [1–3]. Complex structures are stabilized to accomplish the need to approximate a closed electronic outer shell envelope by balancing two-center, two-electron (2c2e) conventional bonds and highly delocalized configurations like three-center, two-electrons (3c2e) bonds. Thus, the predominant three-dimensional bonding character of bulk boron suggests in principle minimal potential for a plain 2D growth. On the contrary, the good stability of small B clusters provides evidence that it is potentially possible to from planar B structures, despite the complexities of the 3D bulk counterpart discussed above [1, 4].

Starting from these considerations, the stability of a number of 2D boron structures has been successfully investigated within the framework of a computational approach, ranging from triangular to honeycomb 2D lattices. It was found that a planar boron sheet can be stabilized in principle when hexagonal vacancies (hexagonal holes—HH) are created in a triangular 2D B framework. The sheet properties vary as a function of the holes' density (η_{HH}) and of their lattice distribution, with sheet geometries spanning from high density buckled structures to a planar honeycomb monolayer, all falling within a narrow stability energy window. Experimentally, these 2D sheets, namely borophene phases, are metastable and need a supporting substrate

for best stabilization through bonding and charge doping in the monolayer regime [5–10], while other stable allotropes can be observed for thicker (multilayer) films as in the cases of Mo and Ni substrates [11, 12]. In the former (monolayer) case, at variance with other growth substrates like e.g. silver [13–17], copper [13, 18–20] and gold [21], a purely honeycomb borophene (hB) phase ($\eta_{HH} = 1/3$) could be stabilized on the Al(111) termination [16, 22–24], where at least 0.5 e$^-$ (0.7 e$^-$/atom in this practical case) are transferred from the substrate to each B atom of the borophene monolayer. In principle, one could categorize borophenes at surfaces by classifying them into three subgroups. A first case is the Ag(111) termination [13–17], where a variety of co-existing B phases is observed, sharing a common triangular structure but with different HH densities and periodicities, yielding moiré coincidence patterns of both rotationally commensurate and incommensurate phases. A second case is represented by *e.g.* the Cu(111) [13, 18–20] and Au(111) [21] surfaces, for which formation of borophene monolayers is strictly connected with the bulk dilution, alloying, and surface segregation of B atoms in the respective metals. Finally, the third case is the Al(111) termination [16, 22–24]. Here, a long-range ordered hB phase can be obtained, hosting, as predicted, Dirac fermions and showing interesting, peculiar electronic properties. However, the strong B–Al interaction that allows the charge transfer to the B layer necessary to stabilize the hB phase is also responsible for the effective formation of a strongly coupled AlB$_2$ layer, involving complex growth mechanisms [25]. Decoupling of the borophene monolayer from the Al substrate in the perspective of exfoliation is quite puzzling, and weakening of the B–Al bond is hard to achieve even by exploiting oxidation or reduction processes [25, 26]. In this work we pursue the idea of diluting Al to weaken the B–Al interaction, while keeping sufficient charge doping of the boron layer in order to maintain the borophene stability. To this purpose, we chose the Ni$_3$Al(111) termination as B deposition and borophene growth substrate. As we will show in the following, however, while B-induced structures form locally in the topmost surface layer, the role of Ni becomes predominant underneath, actually determining a system where alloying and segregation dominate, in close resemblance to the copper and gold cases.

2. Methods

The Ni$_3$Al(111) single crystal surface (Mateck) was prepared by cycles of ion bombardment with Ar$^+$ (2.5 keV—Eurovac ion gun) at room temperature and annealing (1175 K) for 2 min. Heating to high temperature promotes surface geometric and chemical reordering, inducing surface segregation of Al to compensate its higher sputtering cross section with respect to Ni [27]. A sharp $p(2 \times 2)$ low energy electron diffraction (LEED) pattern was obtained in this way (figures S1(a)–(d)), associated with the chemical order of the first surface layer [28]. Boron was then deposited from a physical vapor phase obtained by sublimation of a pure B rod (5 mm diameter, 99.6% purity, Goodfellow). The target was heated by electron bombardment (1 keV, 50 mA) in a home-made metal evaporator. The deposition rate (0.07 ML min^{-1}) was achieved in a residual background pressure in the low 10^{-10} mbar (after several hours of initial outgassing of the source in ultra-high vacuum (UHV)) and calibrated by means of a combination of quartz microbalance, x-ray photoelectron spectroscopy (XPS), and Auger spectroscopy measurements.

The preliminary LEED and Auger characterization of the B/Ni$_3$Al(111) system was performed in a UHV setup available at the Physics Department of the University of Trieste with a base pressure of 5 × 10^{-11} mbar and hosting standard surface science preparation and characterization techniques (including OCI LEED optics and Auger spectrometer) [29]. XPS and scanning tunneling microscopy (STM) measurements were instead performed at the PEARL X03DA beamline of the Swiss Light Source synchrotron radiation facility at the Paul Scherrer Institute (PSI) [30], accessed through proposal submission to the European NFFA consortium. All XPS spectra were collected at room temperature and normal emission. After subtraction of a linear background, best fitting and deconvolution of the spectra through a global least-square minimization approach was accomplished by exploiting Doniach-Šunjič lineshapes [31], convoluted with Gaussian envelopes to account for the thermal, inhomogeneity, and energy resolution broadenings.

3. Results and discussion

3.1. Boron deposition
Deposition and growth of boron on the Ni$_3$Al(111) surface was accomplished by choosing the substrate temperature and the B deposition rate so to promote ordering. Deposition of 2 ML of B at 500 K maintains the sharp $p(2 \times 2)$ symmetry of the LEED pattern (figures S1(a)–(c)), associated with the surface chemical and structural order, which is therefore preserved. Only through energy-dependent (I–V) closer insight (figure S1(c)) it becomes clear that the surface structure has been altered without affecting the periodicity, nor compromising the local surface order (width of the diffraction spots). Figure 1 reports the XPS core level spectra collected in UHV at room temperature for three selected growth conditions (0.7 and 1.6 ML at
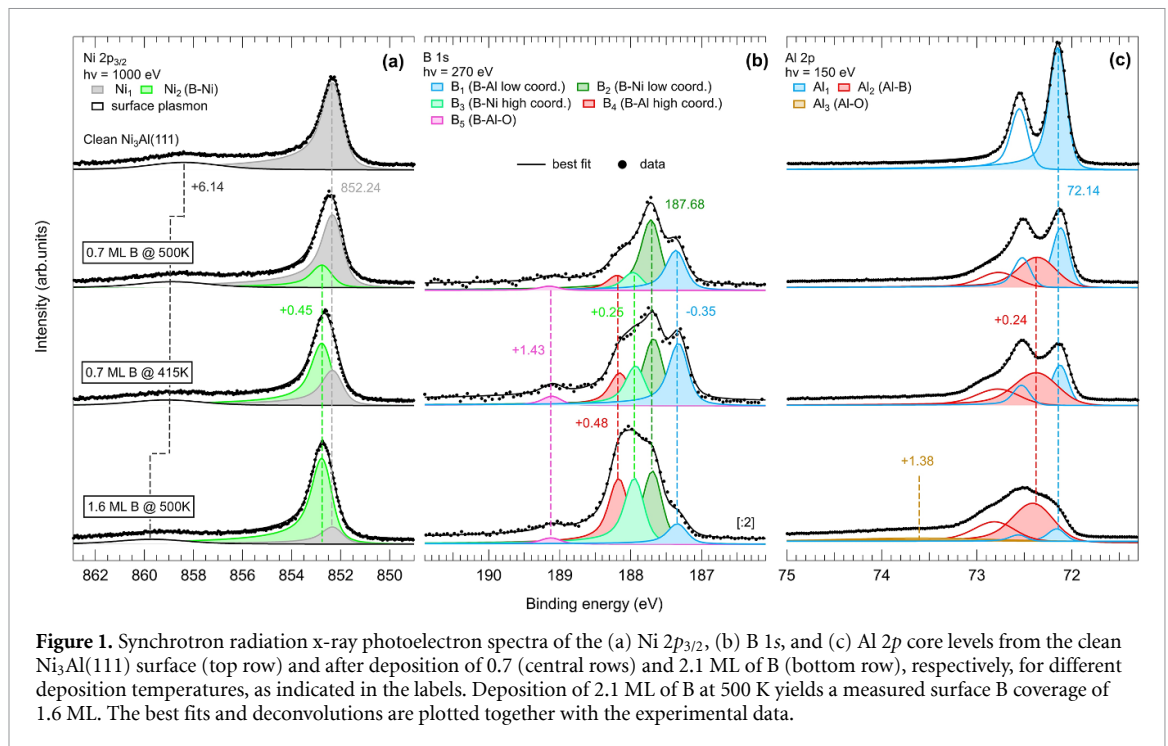
Figure 1. Synchrotron radiation x-ray photoelectron spectra of the (a) Ni $2p_{3/2}$, (b) B $1s$, and (c) Al $2p$ core levels from the clean Ni$_3$Al(111) surface (top row) and after deposition of 0.7 (central rows) and 2.1 ML of B (bottom row), respectively, for different deposition temperatures, as indicated in the labels. Deposition of 2.1 ML of B at 500 K yields a measured surface B coverage of 1.6 ML. The best fits and deconvolutions are plotted together with the experimental data.

500 K, 0.7 ML at 415 K) compared with the bare substrate case. As a general consideration, while several B-induced spectroscopic features appear in the Ni $2p_{3/2}$, B $1s$, and Al $2p$ core level spectra, their binding energies are scarcely affected by the growth conditions (B coverage and surface temperature), at variance with their intensities, which are strongly influenced instead. In detail, we observe that the interaction of B with the alloy termination is associated with the growth of a Ni $2p_{3/2}$ component (Ni$_2$—green) shifted by 0.45 eV to higher binding energy with respect to the main bulk feature (Ni$_1$—grey) at 852.24 eV (figure 1(a)). The plasmonic resonance at +6.14 eV shifts to +6.61 eV and up to + 7.45 eV, depending on the synthesis conditions of the B ad-layer. Similar to the Ni case (figure 1(c)), the Al $2p$ core level spin-orbit doublet (Al$_1$—cyan, separation 0.405 eV, Al $2p_{3/2}$ position at 72.14 eV) gives in intensity to a B-induced doublet at +0.24 eV (Al$_2$—red). A hardly visible shoulder appears at +1.38 eV due to the presence of minor contaminant Al oxide species accumulating at the surface during the longest B deposition (Al$_3$—yellow). Summarizing, both Al and Ni core level spectra show a single, B-induced additional component. Instead, already at first sight, the B $1s$ spectrum (figure 1(b)) appears quite complex, showing a variety of features with different relative intensities, depending on the surface preparation recipe. More specifically, a dominant component grows at 187.68 eV (B$_2$—dark green) for the lowest B surface coverage and growth temperature, accompanied by three other peaks at −0.35 (B$_1$—cyan), +0.25 (B$_3$—light green), and +0.48 eV (B$_4$—red), respectively. A small shoulder (B$_5$—magenta) appears at +1.43 eV, associated with minor O-induced surface contamination due to the long B deposition times (0.07 ML min^{-1}, up to 30 min for the samples of figure 1). While the core level shifts do not vary, the synthesis conditions of the B ad-layer affect the relative intensities of the spectroscopic features. From an absolute intensity point of view, we find that the overall B coverage (extrapolated from a comparison between the cross-section-weighted B $1s$, Al $2p$, and Ni $2p$ peak areas at different photon energies) is not proportional to the amount of the evaporated boron. When deposited at 500 K (last row of figure 1), >2 ML of B yield an actual surface coverage of only 1.6 ML, strongly supporting partial dilution of B into the bulk of Ni$_3$Al. Focusing on the relative intensities, it is observed that the B$_{2-3}$ components behave in line with the Ni$_2$ peak, being more intense when depositing 0.7 ML of B at 415 K than at 500 K, and in the case of higher B loadings (1.6 ML). We thus relate B$_2$ and B$_3$ contributions to B–Ni bonds. Furthermore, as a general rule based on the initial state of the photoemission process, it is accepted that higher B coordination numbers reflect in higher B $1s$ binding energies [16], following a trend observed also for C atoms in graphene [32]. Following this assumption, we assign B atoms contributing to B$_3$ to more coordinated bonding geometries with respect to those contributing to B$_2$. Analogously, the intensity behavior of B$_4$ well-correlates with the Al$_2$ features, suggesting a relation with B–Al bonds. In fact, we observe weak dependence on the growth temperature, and a strong relation with the B loading. B$_4$ is the most shifted component, thus indicating highest coordination. B$_1$ is then associated with a low coordination geometry of the B ad-atoms, in line with its intensity decrease for higher B coverage.
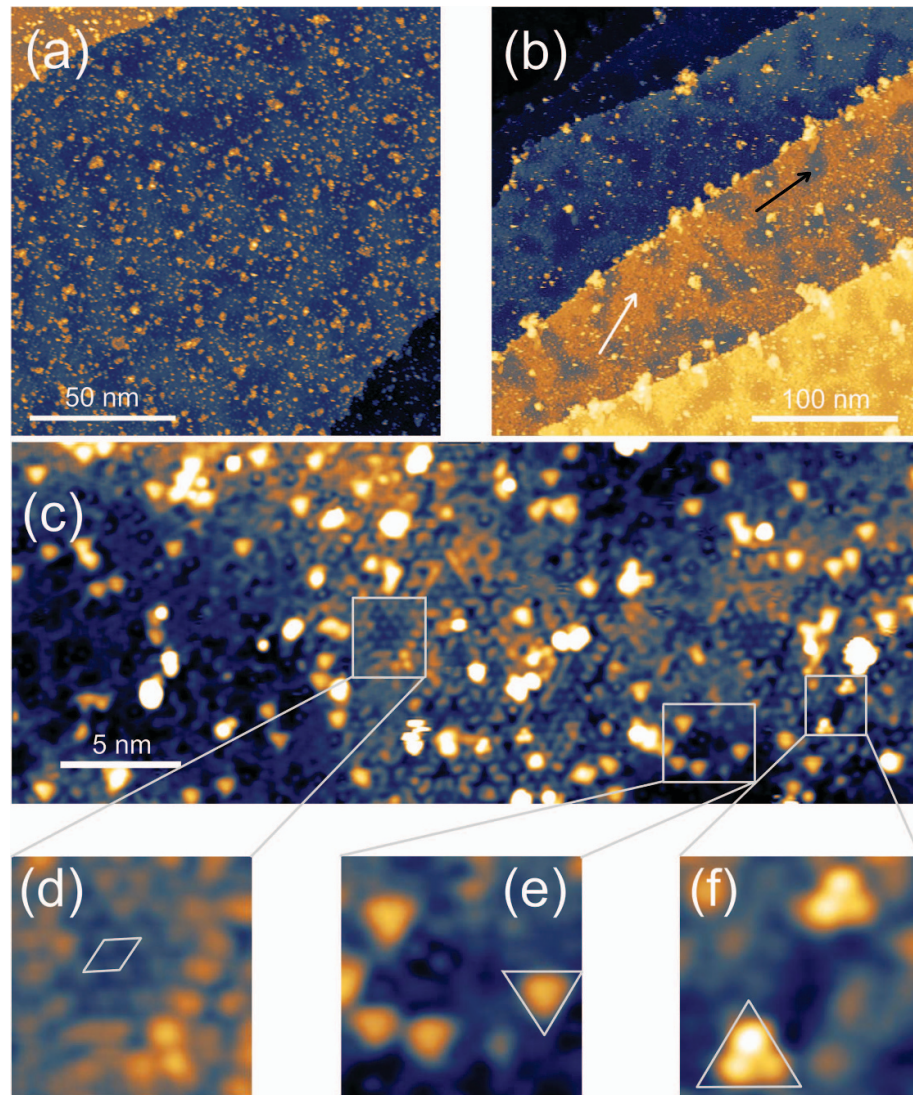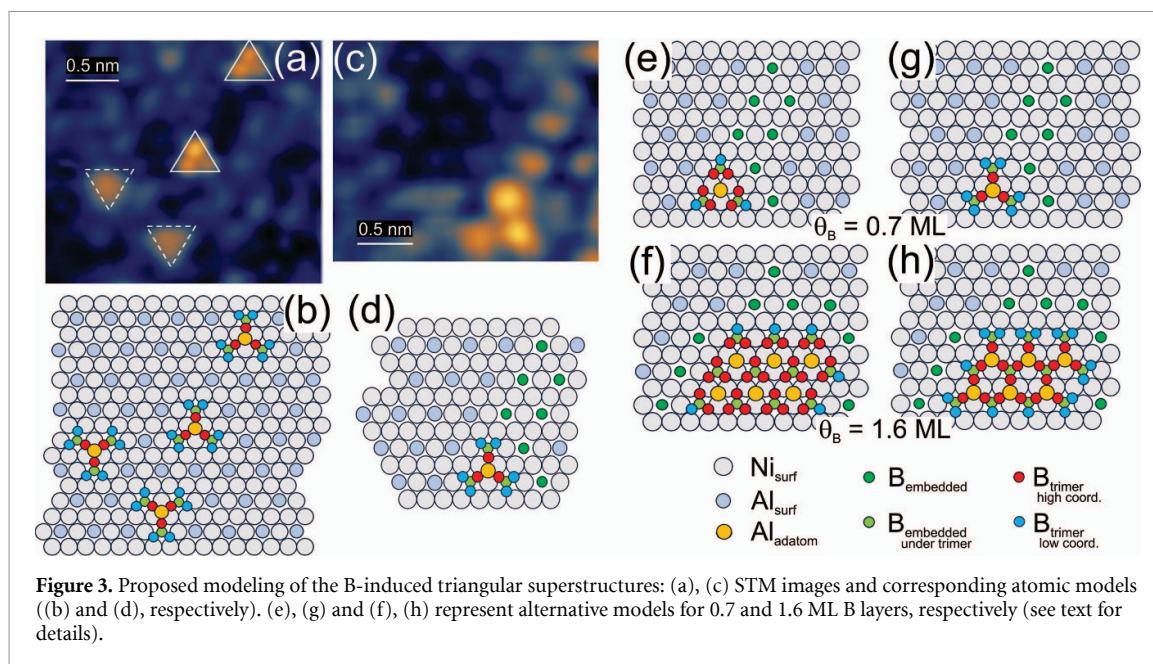
Figure 2. (a)–(c) STM images collected at LHe temperature of 0.7 ML B/Ni$_3$Al(111) deposited at 490 K with a rate of 0.07 ML min^{-1} [(a) $I = 100$ pA, $V = -0.8$ V; (b) $I = 100$ pA, $V = -2.0$ V; (c) $I = 0.3$ nA, $V = -0.5$ V]; (d) sub-region of image (c) displaying a clean Ni$_3$Al(111) area (the (2 × 2) unit cell is depicted) and embedded B atoms (brighter spots); (e)–(f) non-equivalent triangular superstructures.

In figure 2 we plot a selection of STM images obtained at liquid helium temperature after depositing 0.7 ML of B (0.07 ML min^{-1}, 10 min) on the sample held at 500 K. Panels (a) and (b) of the figure show large scale areas of the surface, from which it is clear at first glance that no long-range ordered superstructure is formed, apparently. Few B clusters are uniformly and randomly widespread over the surface, with a broad size distribution centered at about 1 nm diameter, not exceeding 10 nm, and a preference for seeding larger clusters at step edges. However, the surface shows large areas (tens of nm) appearing with different (dark and bright) contrast upon imaging (best evident in figure 2(b)), with a very different local structure, as evidenced by closer inspection (figure 2(c)). More specifically, the darker areas (black arrow) of each terrace correspond to residual clean portions of the Ni$_3$Al(111) termination, in agreement with previous observations [27, 33, 34], where achievement of atomic resolution and clear cut imaging of the $p(2 \times 2)$ phase is quite puzzling due to the presence of distorting charge density waves and chemical disorder. Nevertheless, the 5.03 Å periodicity of the surface unit cell could be observed and measured locally, confirming the known Al–Al distance (the unit cell is depicted in figure 2(d)). In addition to the clean surface pattern, the bright areas (white arrow in figure 2(c)) of the surface show instead at least three B-induced local structures, embedded in the topmost surface layer (figure 2(d)) or decorating the termination as ad-structures (panels (e) and (f)), matching the $p(2 \times 2)$ periodicity and thus supporting the observed LEED pattern. The bright protrusions visible in figure 2(d) are in phase and in plane with the surface Al atoms sites at the corners of the $p(2 \times 2)$ cell and can be associated with substitutional B atoms in the terminal surface layer. While the measured corrugation induced by the Al atoms of the clean Ni$_3$Al(111) surface amounts to 5 pm, the substitutional B

Figure 3. Proposed modeling of the B-induced triangular superstructures: (a), (c) STM images and corresponding atomic models ((b) and (d), respectively). (e), (g) and (f), (h) represent alternative models for 0.7 and 1.6 ML B layers, respectively (see text for details).

atoms induce a corrugation of 20 pm. The triangular shapes evidenced in panels (e) and (f), instead, can be associated with ad-structures, with height profiles well-exceeding 1 Å and a side length equal to the $p(2 \times 2)$ lattice vector. Moreover, we can distinguish between two non-equivalent triangles with the tip pointing downwards (panel (e)) and upwards (panel (f)) in the respective images. At variance with the former, in the latter case internal resolution could be achieved, showing the presence of three self-assembled protrusions.

On the basis of the spectroscopy and microscopy information collected up to here, we can put forward tentative structural models that are compatible with the observations. In figure 3 we reproduce the STM imaging of selected areas (panels (a) and (c)) associated with their proposed modeling (panels (b) and (d)) and then extend the models to a locally higher B coverage (panels (e)–(g) and (f)–(h), respectively), which is simply obtained with a higher density of the triangular units. This is inferred from the relative intensities measured for the B_{1-4} components in the corresponding B 1s XPS core level spectra reported in figure 1(b). For better direct comparison, the plots have been merged in figure S2. The structure nucleation sites consist in the $p(2 \times 2)$ of embedded B atoms (dark green) that are substitutional to Al in (at least) the first Ni$_3$Al layer, directly imaged by STM and associated with the B_2 component of the B 1s core level. B trimers nucleate at these sites, reasonably stabilized by a coordinating Al ad-atom (yellow). The underlying B atom of the surface, acting as a seed, increases its coordination (light green) thus contributing now to the B_3 component in the B 1s spectra, while the trimer B ad-atoms are associated with the B_1 (cyan, low coordination) and B_4 (red, high coordination) components, respectively. The two non-equivalent triangular strictures can be obtained from the re-orientation of the B trimers originating from the direct coordination to the Al ad-atoms. A role could also be played by adsorption at the *hcp* or *fcc* sites of the $p(2 \times 2)$-Al structure of the substrate, respectively. Following this model, the B–Ni and B–Al coordination evidenced in the Ni and Al 2p core level spectra is also reproduced.

3.2. Boron oxidation

To investigate boron oxidation on the Ni$_3$Al(111) termination, we adopted three complementary approaches: (i) boron deposition in UHV and post oxidation by exposure to O$_2$, (ii) boron deposition in O$_2$ background, and (iii) boron deposition on the ultra-thin Al$_2$O$_3$/Ni$_3$Al(111) oxide film. In the latter case, the oxide film was synthesized by high temperature oxidation of the bare alloy single crystal surface in O$_2$ background following established recipes, obtaining an extremely sharp characteristic LEED pattern (figure S1(e)) showing the typical ($\prod67 \times \prod67$)-R12.2° unit cell [35–43]. When depositing B on this film, no B-induced surface order was observed in LEED, while degradation of the diffraction pattern of the superstructure was evident instead (figure S1(e′)). Interestingly, procedures (i) and (ii) led to boron oxidation, at variance with what was observed for the AlB$_2$ layer on Al(111), where the metal substrate was selectively oxidized [25]. For low exposures (of the order of 10 L), the B/Ni$_3$Al(111) layer maintains the $p(2 \times 2)$ symmetry, in spite of a progressive degradation of the diffraction pattern (figures S1(d), (d′) and (d″)). The effects of oxidation are already evident from the Auger spectroscopy measurements (figure S3), showing that Ni is not involved, while both B and Al surface oxide phases are formed. Post-exposure of 2 ML B/Ni$_3$Al(111) at room
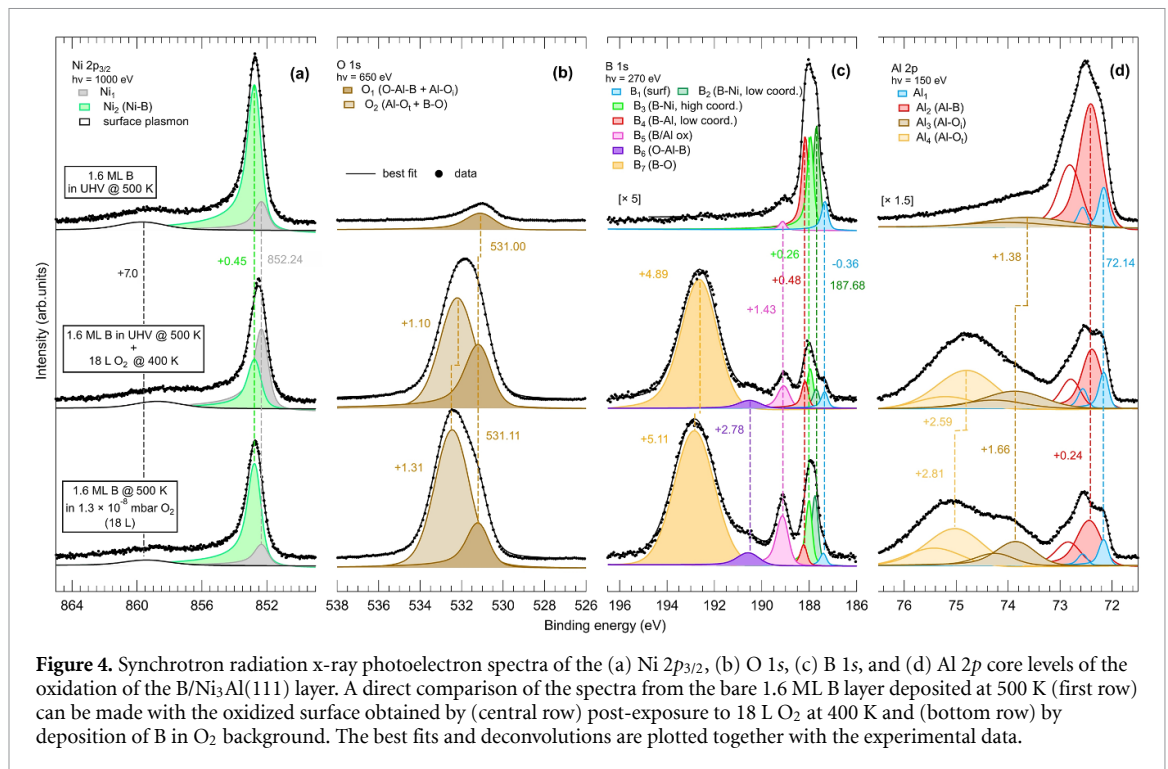
Figure 4. Synchrotron radiation x-ray photoelectron spectra of the (a) Ni $2p_{3/2}$, (b) O $1s$, (c) B $1s$, and (d) Al $2p$ core levels of the oxidation of the B/Ni$_3$Al(111) layer. A direct comparison of the spectra from the bare 1.6 ML B layer deposited at 500 K (first row) can be made with the oxidized surface obtained by (central row) post-exposure to 18 L O$_2$ at 400 K and (bottom row) by deposition of B in O$_2$ background. The best fits and deconvolutions are plotted together with the experimental data.

temperature to increasing amounts of background O$_2$ up to a cumulative dose of 36 L induces according shifts in the Auger KLL transitions witnessing oxidation [44–47]: from 65 to 50 eV for Al, from 178 to 168 and 152 eV for B, accompanied by the growth of atomic oxygen KLL modulations at 510 (KVV ^{1}D) and 488 (KL$_1$V ^{1}P) eV. The oxidation process is best evident from the XPS core level spectra, providing finer details. In figure 4 we report the direct comparison between the Ni $2p_{3/2}$ (panel (a)), O $1s$ (panel (b)), B $1s$ (panel (c)), and Al $2p$ (panel (d)) core level spectra collected on the pristine B/Ni$_3$Al(111) layer (nominal 2 ML of B, effective 1.6 ML of surface B, first row), after post-oxidation with 18 L O$_2$ at 400 K (central row), and upon deposition of B in O$_2$ background at 500 K (total O$_2$ dose 18 L). Already at a first glance we can catch two relevant pieces of information from the spectra: (i) nickel is not oxidized (figure 4(a)) at variance with both boron and aluminum, confirming the Auger spectroscopy data; (ii) oxygen induces surface segregation of B, as evident from the B $1s$ peak areas in panel (c) of the figure (the spectrum in the topmost panel is multiplied by a factor of 5). Moreover, the intensity ratio of the Ni$_1$ and Ni$_2$ components is reversed in the cases of post-oxidation and B deposition in O$_2$ background, suggesting B segregation is further favored in the former case. The O $1s$ spectrum (figure 4(b)) reveals the presence of two broad, mostly gaussian features, associated with surface inhomogeneity broadening, at 531.1 and 532.2–532.4 eV. According to literature [43, 45], the low energy peak can be attributed to interfacial Al–O bonds of an Al oxide film and to a ternary O–Al–B phase, while the high energy peak originates from terminal Al–O species and boron oxide [48]. The Al $2p$ spectrum (figure 4(d)) confirms oxidation of the Ni$_3$Al(111) termination towards the initial formation of an ultra-thin alumina oxide film [43], with two new Al $2p$ spin orbit doublets growing at +1.66 and +2.59/+2.81 eV from the bulk reference, associated with interface and terminal Al–O species, respectively. The B $1s$ spectrum reveals the presence of two additional components with respect to B$_{1-5}$ that can be observed upon growth of the bare B system. Specifically (figure 4(c)), a minor feature appears at 190.5 eV (violet), while a very intense peak dominates at 192.6–192.8 eV (yellow), associated with ternary Al–B–O and B oxide phases, respectively [25, 48].

4. Conclusions

The role of the boron-substrate interaction is fundamental for the synthesis of 2D borophene phases due to the stabilization effect provided by charge doping. However, too strong interactions may lead to B solubility into the support, as for copper and gold, or to the formation of strongly coupled boron-metal bilayers, as in the case of aluminum. The Ni$_3$Al(111) termination can be seen in this sense as a diluted Al surface, where 0.25 ML of Al atoms are arranged in a $p(2 \times 2)$ geometry dispersed by nickel. We find that deposition of B from physical vapor on this termination does not yield to the formation of long range ordered superstructures. Nevertheless, boron assembles in dispersed clusters and in locally ordered nanostructures

pinned by what we propose to be substitutional boron atoms in the $p(2 \times 2)$-Al surface lattice. Spectroscopic insight reveals multiple local coordination geometries for boron, showing the prevalence of B trimers as structural building blocks. B dilution into the Ni$_3$Al bulk is evident, with segregation to the surface promoted by oxidation. Exposure of the B layer to background oxygen or co-deposition of B in oxygen background yield the formation of aluminum and boron surface oxides. A structural coordination model is proposed that is compatible with the reported spectroscopic and microscopic experimental data. Validation by means of computational approaches will be then necessary.

Data availability statements

The data that support the findings of this study are openly available at the following URL/DOI: discovery.psi.ch. Data will be available from 01 November 2025.

Acknowledgments

ORCID iDs

M K Muntwiler ● https://orcid.org/0000-0002-6628-3977
E Vesselli ● https://orcid.org/0000-0002-6799-0032

References

[1] Sergeeva A P, Popov I A, Piazza Z A, Li W-L, Romanescu C, Wang L-S and Boldyrev A I 2014 Understanding boron through size-selected clusters: structure, chemical bonding, and fluxionality *Acc. Chem. Res.* **47** 1349–58
[2] Shirai K 2017 Phase diagram of boron crystals *Jpn. J. Appl. Phys.* **56** 05FA06
[3] Matsuda I and Wu K 2021 *2D Boron: Boraphene, Borophene, Boronene* (Springer International Publishing)
[4] Piazza Z A, Hu H-S, Li W-L, Zhao Y-F, Li J and Wang L-S 2014 Planar hexagonal B36 as a potential basis for extended single-atom layer boron sheets *Nat. Commun.* **5** 3113
[5] Yang X, Ding Y and Ni J 2008 Ab initio prediction of stable boron sheets and boron nanotubes: structure, stability, and electronic properties *Phys. Rev.* B **77** 041402
[6] Penev E S, Bhowmick S, Sadrzadeh A and Yakobson B I 2012 Polymorphism of two-dimensional boron *Nano Lett.* **12** 2441–5
[7] Wu X, Dai J, Zhao Y, Zhuo Z, Yang J and Zeng X C 2012 Two-dimensional boron monolayer sheets *ACS Nano* **6** 7443–53
[8] Wang V and Geng W T 2017 Lattice defects and the mechanical anisotropy of borophene *J. Phys. Chem.* C **121** 10224–32
[9] Xu S-G, Li X-T, Zhao Y-J, Liao J-H, Xu W-P, Yang X-B and Xu H 2017 Two-dimensional semiconducting boron monolayers *J. Am. Chem. Soc.* **139** 17233–6
[10] Zhang Z, Shirodkar S N, Yang Y and Yakobson B I 2017 Gate-voltage control of borophene structure formation *Angew. Chem., Int. Ed.* **56** 15421–6
[11] Wang X, Tai G, Wu Z, Hu T and Wang R 2017 Ultrathin molybdenum boride films for highly efficient catalysis of the hydrogen evolution reaction *J. Mater. Chem.* A **5** 23471–5
[12] Wu Z, Tai G, Shao W, Wang R and Hou C 2020 Experimental realization of quasicubic boron sheets *Nanoscale* **12** 3787–94
[13] Liu Y, Penev E S and Yakobson B I 2013 Probing the synthesis of two-dimensional boron by first-principles computations *Angew. Chem., Int. Ed.* **52** 3156–9
[14] Mannix A J *et al* 2015 Synthesis of borophenes: anisotropic, two-dimensional boron polymorphs *Science* **350** 1513–6
[15] Mannix A J, Zhang Z, Guisinger N P, Yakobson B I and Hersam M C 2018 Borophene as a prototype for synthetic 2D materials development *Nat. Nanotechnol.* **13** 444–50
[16] Feng B, Zhang J, Zhong Q, Li W, Li S, Li H, Cheng P, Meng S, Chen L and Wu K 2016 Experimental realization of two-dimensional boron sheets *Nat. Chem.* **8** 563–8
[17] Campbell G P, Mannix A J, Emery J D, Lee T-L, Guisinger N P, Hersam M C and Bedzyk M J 2018 Resolving the chemically discrete structure of synthetic borophene polymorphs *Nano Lett.* **18** 2816–21
[18] Wu R, Gozar A and Božović I 2019 Large-area borophene sheets on sacrificial Cu(111) films promoted by recrystallization from subsurface boron *npj Quantum Mater.* **4** 40
[19] Yue C *et al* 2021 Formation of copper boride on Cu(111) *Fundam. Res.* **1** 482–7
[20] Li H *et al* 2023 Monolayer borophene formation on Cu(111) surface triggered by (1–10) step edge *Small* 2303502
[21] Kiraly B, Liu X, Wang L, Zhang Z, Mannix A J, Fisher B L, Yakobson B I, Hersam M C and Guisinger N P 2019 Borophene synthesis on Au(111) *ACS Nano* **13** 3816–22
[22] Shirodkar S N, Penev E S and Yakobson B I 2018 Honeycomb boron: alchemy on aluminum pan? *Sci. Bull.* **63** 270–1
[23] Li W, Kong L, Chen C, Gou J, Sheng S, Zhang W, Li H, Chen L, Cheng P and Wu K 2018 Experimental realization of honeycomb borophene *Sci. Bull.* **63** 282–6
[24] Preobrajenski A B, Lyalin A, Taketsugu T, Vinogradov N A and Vinogradov A S 2021 Honeycomb boron on Al(111): from the concept of borophene to the two-dimensional boride *ACS Nano* **15** 15153–65

[25] Biasin P *et al* 2023 Growth and redox properties of borophene: competing affinities in the case of honeycomb AlB2/Al(111) submitted

[26] Biasin P, Safari M, Ghidorsi E, Baronio S, Scardamaglia M, Preobrajenski A, de Gironcoli S, Baroni S and Vesselli E 2023 From borophene polymorphs towards a single honeycomb borophane phase: reduction of hexagonal boron layers on Al(111) *Nanoscale* **15** 18407–14

[27] Bikondoa O, Castro G R, Torrelles X, Wendler F and Moritz W 2005 Surface-induced disorder on the clean Ni₃Al(111) surface *Phys. Rev.* B **72** 195430

[28] Vesselli E, Bianchettin L, Baraldi A, Sala A, Comelli G, Lizzit S, Petaccia L and de Gironcoli S 2008 The Ni₃Al(111) surface structure: experiment and theory *J. Phys.: Condens. Matter* **20** 195223

[29] Corva M, Feng Z, Dri C, Salvador F, Bertoch P, Comelli G and Vesselli E 2016 Carbon dioxide reduction on Ir(111): stable hydrocarbon surface species at near-ambient pressure *Phys. Chem. Chem. Phys.* **18** 6763–72

[30] Muntwiler M *et al* 2017 Surface science at the PEARL beamline of the swiss light source *J. Synchrotron Radiat.* **24** 354–66

[31] Doniach S and Sunjic M 1970 Many-electron singularity in x-ray photoemission and x-ray line spectra from metals *J. Phys. C: Solid State Phys.* **3** 285–91

[32] Susi T, Kaukonen M, Havu P, Ljungberg M P, Ayala P and Kauppinen E I 2014 Core level binding energies of functionalized and defective graphene *Beilstein J. Nanotechnol.* **5** 121–32

[33] Jurczyszyn L, Krupski A, Degen S, Pieczyrak B, Kralj M, Becker C and Wandelt K 2007 Atomic structure and electronic properties of Ni₃Al (111) and (011) surfaces *Phys. Rev.* B **76** 045101

[34] Jurczyszyn L, Rosenhahn A, Schneider J, Becker C and Wandelt K 2003 Formation of STM images of Ni₃Al (001) and (111) surfaces *Phys. Rev.* B **68** 115425

[35] Rosenhahn A, Schneider J, Becker C and Wandelt K 1999 The formation of Al₂O₃-layers on Ni₃Al(111) *Appl. Surf. Sci.* **142** 169–73

[36] Degen S, Krupski A, Kralj M, Langner A, Becker C, Sokolowski M and Wandelt K 2005 Determination of the coincidence lattice of an ultra thin Al₂O₃ film on Ni₃Al(111) *Surf. Sci.* **576** L57–64

[37] Hamm G, Barth C, Becker C, Wandelt K and Henry C R 2006 Surface structure of an ultrathin alumina film on Ni₃Al(111): a dynamic scanning force microscopy study *Phys. Rev. Lett.* **97** 126106

[38] Becker C, Kandler J, Raaf H, Linke R, Pelster T, Dräger M, Tanemura M and Wandelt K 1998 Oxygen adsorption and oxide formation on Ni₃Al (111) *J. Vac. Sci. Technol.* A **16** 1000–5

[39] Addepalli S G, Ekstrom B, Magtoto N P, Lin J-S and Kelber J A 1999 STM atomic-scale characterization of the γ′-Al₂O₃ film on Ni₃Al(111) *Surf. Sci.* **442** 385–99

[40] Gritschneder S, Degen S, Becker C, Wandelt K and Reichling M 2007 Atomic structure of a stripe phase on Al₂O₃/Ni₃Al(111) revealed by scanning force microscopy *Phys. Rev.* B **76** 014123

[41] Rosenhahn A, Schneider J, Kandler J, Becker C and Wandelt K 1999 Interaction of oxygen with Ni₃Al(111) at 300 K and 1000 K *Surf. Sci.* **433–435** 705–10

[42] Garza M, Magtoto N and Kelber J 2002 Characterization of oxidized Ni₃Al(110) and interaction of the oxide film with water vapor *Surf. Sci.* **519** 259–68

[43] Vesselli E, Baraldi A, Lizzit S and Comelli G 2010 Large interlayer relaxation at a metal-oxide interface: the case of a supported ultrathin alumina film *Phys. Rev. Lett.* **105** 046102

[44] Chen J G, Crowell J E and Yates J T 1986 Onset of oxidation of Al(111) at low temperatures: a study by electron-energy-loss spectroscopy and Auger electron spectroscopy *Phys. Rev.* B **33** 1436–9

[45] Ma X, Kratky T and Günther S 2019 Observation of a novel double layer surface oxide phase on Ni₃ Al(111) at low temperature *Nanoscale Adv.* **1** 4501–12

[46] Joyner D J and Hercules D M 1980 Chemical bonding and electronic structure of B₂O₃, H₃BO₃, and BN: an ESCA, Auger, SIMS, and SXS study *J. Chem. Phys.* **72** 1095–108

[47] Humbert P and Deville J P 1987 Oxygen Auger spectra of some transition-metal oxides: relaxation energies and d-band screening *J. Phys. C: Solid State Phys.* **20** 4679–87

[48] Wang Y and Trenary M 1993 Surface chemistry of boron oxidation. 2. The reactions of boron oxides B₂O₂ and B₂O₃ with boron films grown on tantalum(110) *Chem. Mater.* **5** 199–205